

Article

Functionalization of Violet Phosphorus Quantum Dots with Azo-Containing Star-Shape Polymer for Optically Controllable Memory

Fan Shu [†], Weilin Chen [†] and Gang Liu ^{*}

Department of Micro/Nano Electronics, School of Electronic Information and Electrical Engineering, Shanghai Jiao Tong University, Shanghai 200240, China; woshishufan@sjtu.edu.cn (F.S.); chenweilin@sjtu.edu.cn (W.C.)

* Correspondence: gang.liu@sjtu.edu.cn

[†] These authors contributed equally to this work.

Abstract: Quantum dots (QDs) are emerging as promising candidates for innovative memristive materials, owing to their distinct surface, quantum size, and edge effects. Recent research has focused on tailoring QDs with specific organic molecules to fine-tune charge transfer states between the host and grafted species, as well as enhancing their dispersibility and processability. Violet phosphorus (VP), a newly discovered two-dimensional phosphorus allotrope, offers excellent carrier dynamics, predictable modifiability, and superior oxidation resistance, making it a promising contender in this domain. In this study, we synthesized a rich azobenzene-containing star-shaped polymer diazonium salt (AzoSPD) to functionalize violet phosphorus quantum dots (VPQDs), with the dual objectives of enhancing organic dispersibility and introducing photo-switching capabilities. The synthesized AzoSPD-VPQDs exhibit intramolecular charge transfer characteristics under electrical stimuli of ambient conditions, displaying significant non-volatile rewriteable memory properties and a substantial switching ratio exceeding 2×10^3 . Furthermore, the high resistance state (HRS) current can be enhanced by nearly 40 times under 465 nm illumination, enabling optoelectronic information sensing and storage within a single device. This work not only provides insights into enhancing the optoelectronic properties of QDs through functional organic molecular modification but also represents a pioneering exploration of the potential applications of VPQDs in novel memristors.

Keywords: violet phosphorus quantum dots; star-shape polymer diazonium salt; memristor; charge transfer mechanism; photoelectric regulation



Citation: Shu, F.; Chen, W.; Liu, G. Functionalization of Violet Phosphorus Quantum Dots with Azo-Containing Star-Shape Polymer for Optically Controllable Memory.

Processes **2023**, *11*, 3429. <https://doi.org/10.3390/pr11123429>

Academic Editor: Jih-Hsin Liu

Received: 21 November 2023

Revised: 9 December 2023

Accepted: 13 December 2023

Published: 14 December 2023



Copyright: © 2023 by the authors. Licensee MDPI, Basel, Switzerland. This article is an open access article distributed under the terms and conditions of the Creative Commons Attribution (CC BY) license (<https://creativecommons.org/licenses/by/4.0/>).

1. Introduction

The extremely small size and vast specific surface area endow quantum dots (QDs) with unique quantum confinement effects and abundant active surface sites, offering broad application prospects in the fields of novel electronics and optoelectronics [1–5]. In recent years, black phosphorus (BP) and transition-metal dichalcogenide (TMDC) QDs have emerged as outstanding candidates in the development of novel memristors [6–9]. These QDs can provide satisfying trapping sites during the charge transfer process, leading to significant resistance state changes under bias, enabling the storage of information with rapid access and low power consumption. However, most of the reported work has focused on physically blending QDs with polymer matrices, which can lead to serious phase separation issues that deteriorate device performance. Additionally, traditional graphene, BP, and TMDCs suffer from the challenges of zero band gap, oxidation, and unremarkable carrier dynamics, respectively [10–13]. Therefore, there is an urgent need to develop novel QDs with improved functionalization effects to further advance the development of QD-based memristors.

As a newly discovered two-dimensional material, violet phosphorus (VP) features a moderate band gap (with an optical band gap of approximately 1.7 eV), high carrier mobility ($7000 \text{ cm}^2/(\text{V}\cdot\text{S})$), and better environmental stability compared to BP [14], making it an ideal platform for the development of high-performance memristors. Additionally, the covalent functionalization method offers a well-established approach for fine-tuning the properties of quantum dots (QDs) [15]. Specifically designed organic molecules can not only provide customized performance regulation sites [9,16] but also improve film-forming properties and passivation protection during the device manufacturing process [17–19]. As one of the most extensively investigated photosensitive organic functional groups, azobenzene and its derivatives exhibit an intriguing reversible cis–trans isomerization characteristic, which has the potential to confer specific optically controllable properties to the traditional memory-only QD-based memristor [20,21]. With the continuous evolution of the information era, there is an increasing urgency to develop novel hybrid memristors capable of enabling multi-dimensional information perception and storage [22,23]. The use of azobenzene-based polymers for the covalent functionalization of VPQDs represents a promising strategy to diversify device control methods, streamline the device preparation process, and enhance overall performance.

To this end, a star-shaped polymer diazonium salt (AzoSPD) rich in azobenzene structure was designed and synthesized to covalently functionalize VPQDs. The introduction of a star-shaped polymer and azobenzene brings better solubility, environmental stability, and additional light regulation capability to VPQD-based memristors. Under environmental voltage stimulation, electrons in the AzoSPD moiety delocalize onto the VPQDs, forming the charge transfer state that triggers memristive behaviors. The strong light absorption characteristics and photo-induced configuration transition properties of azobenzene groups in AzoSPD provide an additional control means for the charge transfer pathway, enabling the device to exhibit photoelectric regulation capabilities at the macroscopic level. The modification process is supported by various spectral and theoretical calculations, and the related devices exhibited significant memristive characteristics with a large switch ratio ($>2 \times 10^3$) in ambient conditions. Under 465 nm illumination, the high-resistance state current of the device can be increased by nearly 40 times, achieving the perception and storage of optical information besides the electrical memory. Our research provides a pioneering exploration experience for the application of VPQDs in the memristor field and the implementation of optoelectronic tunable storage research in single devices.

2. Materials and Methods

2.1. Chemicals

Trimesoyl chloride, 3-(bromomethyl) heptane, and *n*-butyl lithium were purchased from Adamas-beta; 4,4-diaminodiphenyl sulfone, sodium nitrite, and aniline were purchased from Shanghai Aladdin Biochemical Technology Co., Ltd. (Shanghai, China); 3-chloropropanol, 48% tetrafluoroborate, and potassium iodide were purchased from Shanghai Meryer (Shanghai, China) Chemical Technology Co., Ltd. (Shanghai, China); sodium bicarbonate and anhydrous calcium chloride were purchased from General-reagent; tetrabutylammonium hexafluorophosphate was purchased from Bide Pharmatech Ltd. (Shanghai, China); bulk violet phosphorus was given by Zhang Jinying's research group from Xi'an Jiaotong University.

Acetone, dichloromethane, ether, chloroform, and anhydrous ethanol were purchased from General-reagent; petroleum ether was purchased from Meryer (Shanghai, China) Chemical Technology Co., Ltd.; N, N-dimethylformamide (DMF) was purchased from Shanghai Aladdin Biochemical Technology Co., Ltd.; triethylamine was purchased from Sinopharm Chemical Reagent Co., Ltd. (Shanghai, China); ethanol (HPLC, $\geq 99.8\%$), *n*-hexane, and ethyl acetate were purchased from Shanghai Macklin Biochemical Co., Ltd. (Shanghai, China); and pure water was produced by a laboratory ultrapure water machine.

2.2. Synthesis of Modified Molecule AzoSPD

2.2.1. Synthesis of Monomer SDBD

A total of 2.48 g of diaminodiphenyl sulfone and 8 mL of 48% tetrafluoroborate were added to a 250 mL flask and stirred magnetically. Sodium nitrite aqueous solution was prepared using 1.5 g NaNO₂ in 5 mL deionized water. This solution was then slowly added dropwise to the flask under stirring and in an ice water bath, causing the solution to turn bluish-white. The reaction was kept below 5 °C and allowed to stand for 30 min. After filtering, the solid was dissolved in acetone to form a yellow paste, and ether was added to recrystallize the diazonium salt. The resulting light yellow solid SDBD weighed 2.08 g, representing a yield of 57.9%. It was then bottled and stored at a low temperature.

2.2.2. Synthesis of Monomer TBTC

Substitution reaction 1: The mixture of 16.2 mL aniline, 5.2 mL 3-chloro-1-propanol, KI (catalyst), and NaHCO₃ (acid binding agent) was heated and stirred at 100 °C for 5 h. The product was extracted with 50 mL ether and NaHCO₃ was added to remove the residual HCl. The extract was dried with anhydrous CaCl₂ for 30 min, and the solvent was removed by rotary evaporation. The obtained viscous liquid was separated by column chromatography to obtain the product. The column chromatography conditions were as follows: the first impurity point was eluted with pure dichloromethane eluent, and then the product 3-(phenylamino) propanol (second point) was eluted with pure ethyl acetate. The green-yellow oily product of 3.89 g was obtained with a yield of 30.95%.

Substitution reaction 2: A quantity of 4.566 g of the product and 5.793 g of 3-(bromomethyl) heptane were dissolved in DMF. The mixture was stirred at 100 °C for 24 h with 3.15 g of NaHCO₃ and 0.996 g of KI added. After the reaction, a large amount of deionized water was added and extracted with chloroform. The emulsification was broken by solid NaHCO₃. The organic layer was dried with anhydrous CaCl₂ for 30 min and the solvent was removed by rotary evaporation. Column chromatography was performed to obtain the product; the first impurity was eluted with a dichloride (petroleum ether = 2:1), followed by the product and unreacted raw material with dichloromethane (ethyl acetate = 2:1). The final product (3-((2-ethylhexyl)(phenyl)amino)propan-1-ol) was brownish-yellow oil, weighing 3.00 g, with a yield of 38.02%.

Synthesis of tris(3-((2-ethylhexyl)(phenyl)amino)propyl) benzene-1,3,5-tricarboxylate (TBTC) by acyl chloride esterification: Trimethoxy chloride (1.328 g) and triethylamine (2.8 mL) were dissolved in 30 mL dichloromethane, and 3-((2-ethylhexyl)(phenyl)amino)propane-1-ol (4.734 g) was dissolved in 60 mL dichloromethane in another container. The former was dripped into the latter solution during stirring in the ice water bath. After 6 h of reaction, the solution was washed with pure water, the solvent was mostly removed by rotary evaporation, and ethanol was used to recrystallize to obtain TBTC. TBTC was then separated from the recrystallization solution via high-speed centrifugation and dried to yield an extremely viscous yellow-green liquid (1.37 g), with a yield of 39.63%.

2.2.3. Synthesis of the Star-Shaped Polymer Diazonium Salt Rich in Azobenzene Structure (AzoSPD)

A total of 0.988 g TBTC was dissolved in a small amount of DMF. The 0.6675 g SDBD was dissolved in another portion of DMF, and the former solution was dropped dropwise under ice water bath conditions (the total DMF was preferably no more than 10 mL). The reaction was performed for more than 5 days. After the reaction, the system solution was poured into a large amount of acetonitrile, standing and waiting for the final product to be precipitated. The product was a red-black viscous body, which was rubber-like after drying. The reaction equation is shown in Figure 1; the existence form of the monomer in AzoSPD is abbreviated as A and B, respectively.

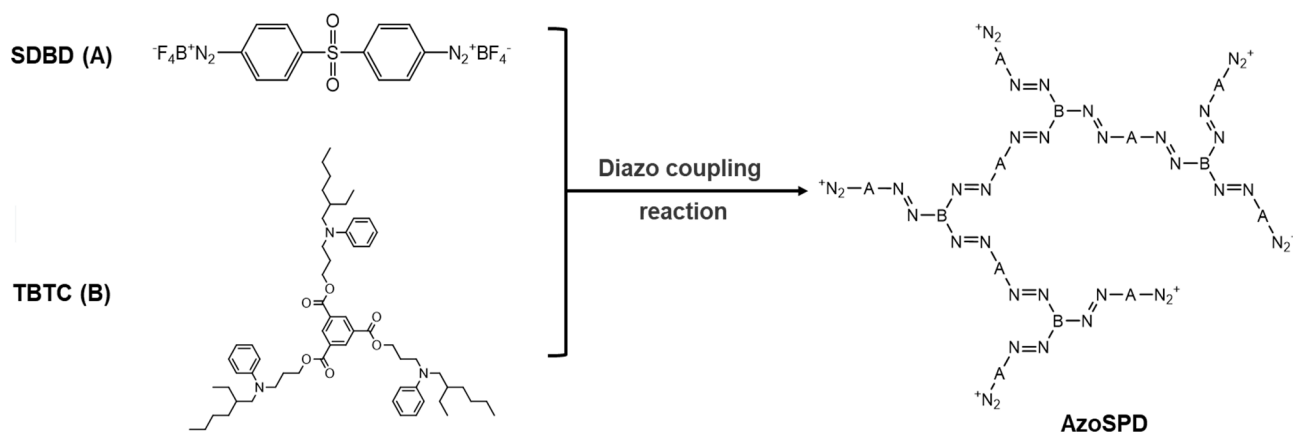


Figure 1. The synthesis reaction equation of AzoSPD: The monomers SDBD and TBTC are polymerized by diazo coupling reaction to obtain AzoSPD, and they exist in AzoSPD in the form of A and B, respectively.

2.3. Preparation and Modification of Violet Phosphorus Quantum Dots (VPQDs)

2.3.1. Stripping of VPQDs

The exfoliation of VPQDs employed classical top-down quantum dot fabrication techniques, including liquid-phase exfoliation and ion-intercalation methods:

Liquid-phase stripping (Figure 2 Reaction (1)): The bulk violet phosphorus was dispersed in high-purity anhydrous ethanol, and continuous ultrasonic treatment was performed using an ultrasonic soundproof box in an ice water bath. Anhydrous ethanol was collected and replaced every 6 h. The collected VP ethanol solution was centrifuged at 13,000 r/min for 1 h and then centrifuged and washed again with deionized water. The precipitate was freeze-dried with a small amount of deionized water to obtain a brownish-yellow powder.

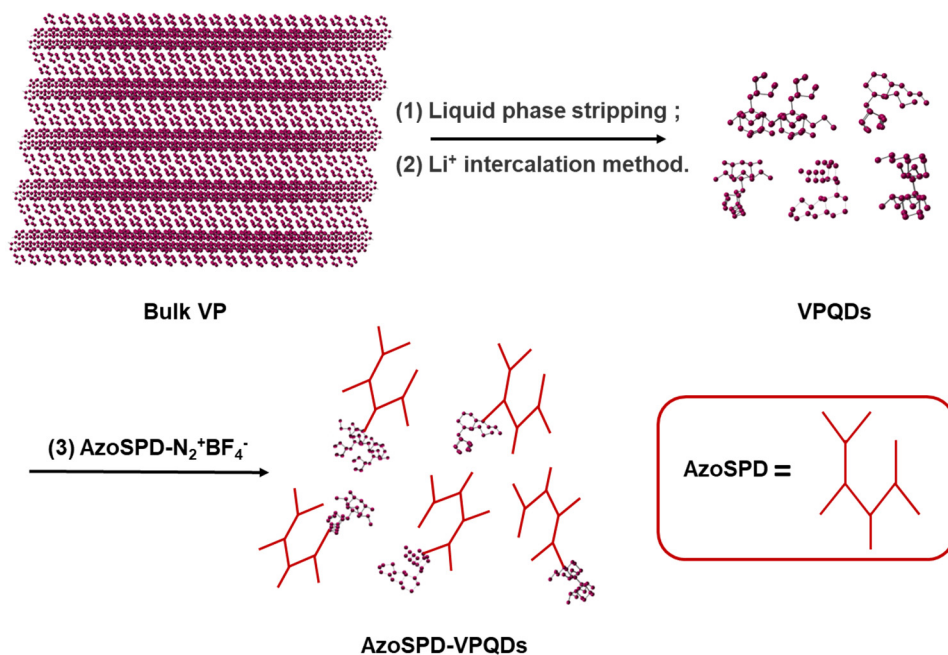


Figure 2. The two-step exfoliation of VPQDs (Reaction (1), (2)) and the surface modification of VPQDs by AzoSPD (Reaction (3)).

Li⁺ intercalation method (Figure 2 Reaction (2)): An amount of 215 mg VP powder was dispersed in n-hexane, and 12 mL of n-butyl lithium was added in an Ar atmosphere. The

mixture was stirred at 75 °C for 40 h to allow the small-sized Li⁺ ions to intercalate between the VP layers. After stirring, the n-hexane was removed by high-speed centrifugation at 13,000 r/min, and chromatographically pure ethanol was added. During the ultrasonication process, the Li⁺ ions intercalated between the VP layers reacted with ethanol to generate a large number of n-butane bubbles, overcoming the van der Waals forces between the VP layers to achieve exfoliation. Once the solution ceased to produce bubbles, the supernatant was collected after centrifugation for 40 min. The VPQD precipitate was then collected at a speed of 15,000 rpm, washed with anhydrous ethanol and deionized water, and then collected after freeze-drying.

2.3.2. Modification of VPQDs

The modification of VPQDs was achieved through the covalent attachment of diazonium salts: A total of 0.2 g AzoSPD was dissolved in 30 mL DMF with 20 mg of VPQDs and 0.581 g tetrabutylammonium hexafluorophosphate and reacted in the dark for 20 h; the reaction diagram is shown in Figure 2 Reaction (3). The reaction solution was centrifuged at 15,000 r/min for 40 min to obtain the modified product AzoSPD–VPQDs. After weighing, it was sealed with quantitative ethanol and refrigerated.

2.4. Device Structure and Fabrication

An ITO-coated conductive glass (10 × 10 × 0.7 mm, 180 nm ITO) was cleaned in pure water, absolute ethanol, and acetone for 15 min each using ultrasound, then dried with N₂. AzoSPD chloroform solution (20 mg/mL) was prepared with AzoSPD as an auxiliary binder. After ultrasonically dispersing the mixture of AzoSPD–VPQDs and ethanol for 3 min, add it to the AzoSPD chloroform solution at a concentration of 0.5 mg/mL. The mixture was again sonicated for 2 min before dropping 100 µL onto the ITO substrate placed in a suction cup of a homogenizer. The spin-coating parameters were 300 r/min 20 s + 2000 r/min 60 s. The sample was then vacuum oven-dried at 60 °C overnight. The top electrode uses a vacuum magnetron coating system to prepare a circular top electrode by electron beam evaporation under the following conditions: Ar gas flow rate of 30 mL/min, growth chamber pressure of 1.3 Pa, and a 30 W RF power supply. The final prepared Au/AzoSPD–VPQD/ITO three-layer structure device is shown in Figure 3. Subsequent tests were performed by powering on both ends of the top electrode Au and the substrate ITO. Scanning electron microscopy (SEM) characterization showed that the thickness of the three layers was about 80 nm, 120 nm, and 180 nm, respectively (Figure S1a), and there are obvious layered element distribution characteristics (Figure S1b).

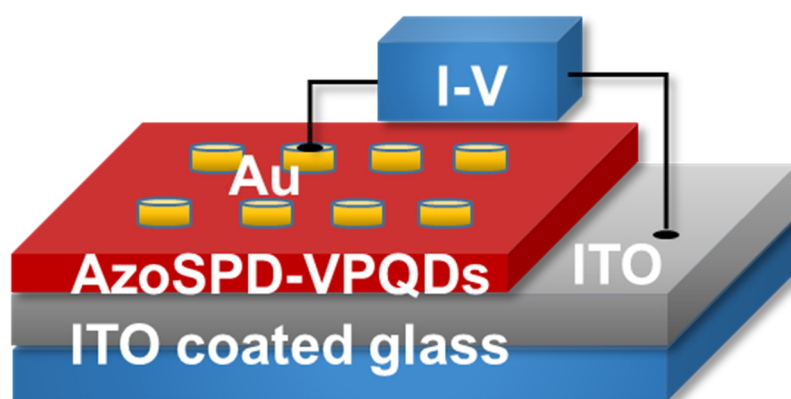


Figure 3. The schematic diagram and test configuration of Au/AzoSPD–VPQD/ITO device. The I–V test is conducted by applying voltage across the top electrode Au and the substrate ITO.

3. Results and Discussion

3.1. Characterization of the VPQDs and AzoSPD–VPQDs

Transmission Electron Microscope (TEM) and Atomic Force Microscope (AFM) morphology characterization methods were used to characterize the size of the prepared samples. Figure 4a,b show the uniform size distribution of VPQDs characterized by TEM and AFM, respectively. The 0.20 nm and 0.21 nm interplanar spacing detected in Figure 4a inset represent the $\{-4,2,4\}$ and $\{3,-3,2\}$ planes of VP, respectively. The measured height of the two lines drawn in Figure 4b are both between 2 and 6 nm (Figure S2). The statistical results show that the average diameter of VPQD is 4.64 ± 0.69 nm and the average height is 5.64 ± 2.16 nm (Figure 4c), suggesting that the van der Waals forces between the VP layers ensure that it still exists in a multilayered form even when reduced to nanoscale dimensions. The TEM of AzoSPD–VPQDs in Figure 4d shows that the modified VPQDs are no longer regular; the obvious branching and long-chain characteristics of AzoSPD are found in high-resolution transmission electron microscopy (HRTEM) in sizes from 20 to 30 nm (Figure 4e). Further amplification can still observe the lattice spacing of 0.20 and 0.29 nm, which belong to the $\{-4,2,4\}$ and $\{-3,1,2\}$ planes of VP, respectively (Figure 4f) [24]. This phenomenon indicates the successful surface bonding between AzoSPD and VPQDs and does not significantly change the crystal structure of VPQDs.

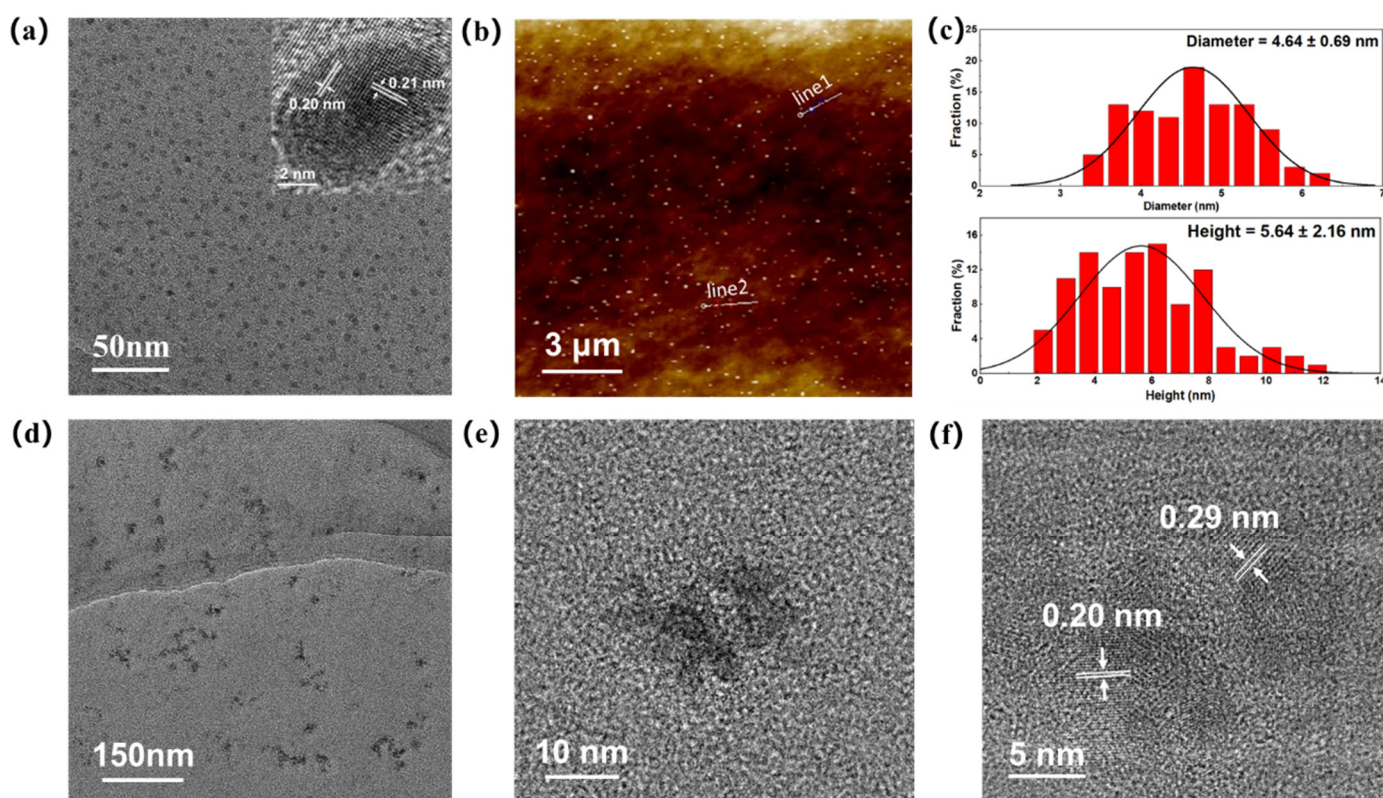


Figure 4. Morphology characterization of VPQDs and AzoSPD–VPQDs. (a) TEM characterization of VPQDs. The inset shows the lattice fringe images under HRTEM; (b) AFM characterization of VPQDs; (c) statistical analysis of the dimensions and heights of VPQDs measured in (a,b); (d) TEM characterization of AzoSPD–VPQDs; (e) HRTEM image of AzoSPD–VPQDs; (f) Further enlarges the lattice fringes shown in (e).

Given the significant differences in elements and bonding after the modification reaction, a variety of spectroscopic characterizations were performed on the prepared samples. In the IR characterization of Figure 5a, the stretching vibration peak of the $-N=N-$ bond generated by polymerization on AzoSPD is located at 1390 cm^{-1} . The large consumption of diazo bonds in the polymerization leads to a significant decrease

in the strength of the stretching vibration peak of the remaining diazo bond ($-N^+ \equiv N^-$) on AzoSPD and the expansion of the conjugated system makes the peak wavenumber shift from 2288 cm^{-1} to 2110 cm^{-1} . The modified product, AzoSPD-VPQDs, has a new absorption peak at 1444 cm^{-1} , corresponding to the Ph-P bond stretching vibration peak of AzoSPD and VP. Figure 5b shows the XPS broad-spectrum scan of AzoSPD-VPQDs and verifies all the elements, including O1s, N1s, C1s, S2s, P2s, S2p, P2p, and O2s, with the binding energies located at 531, 399, 284, 232, 189, 169, 132, and 25 eV, respectively. In addition, the XPS fine spectra fitting results of C1s and P2p in Figure 5c,d both reveal obvious contributions from the C-P bond, providing further evidence for the successful covalent modification of VPQDs.

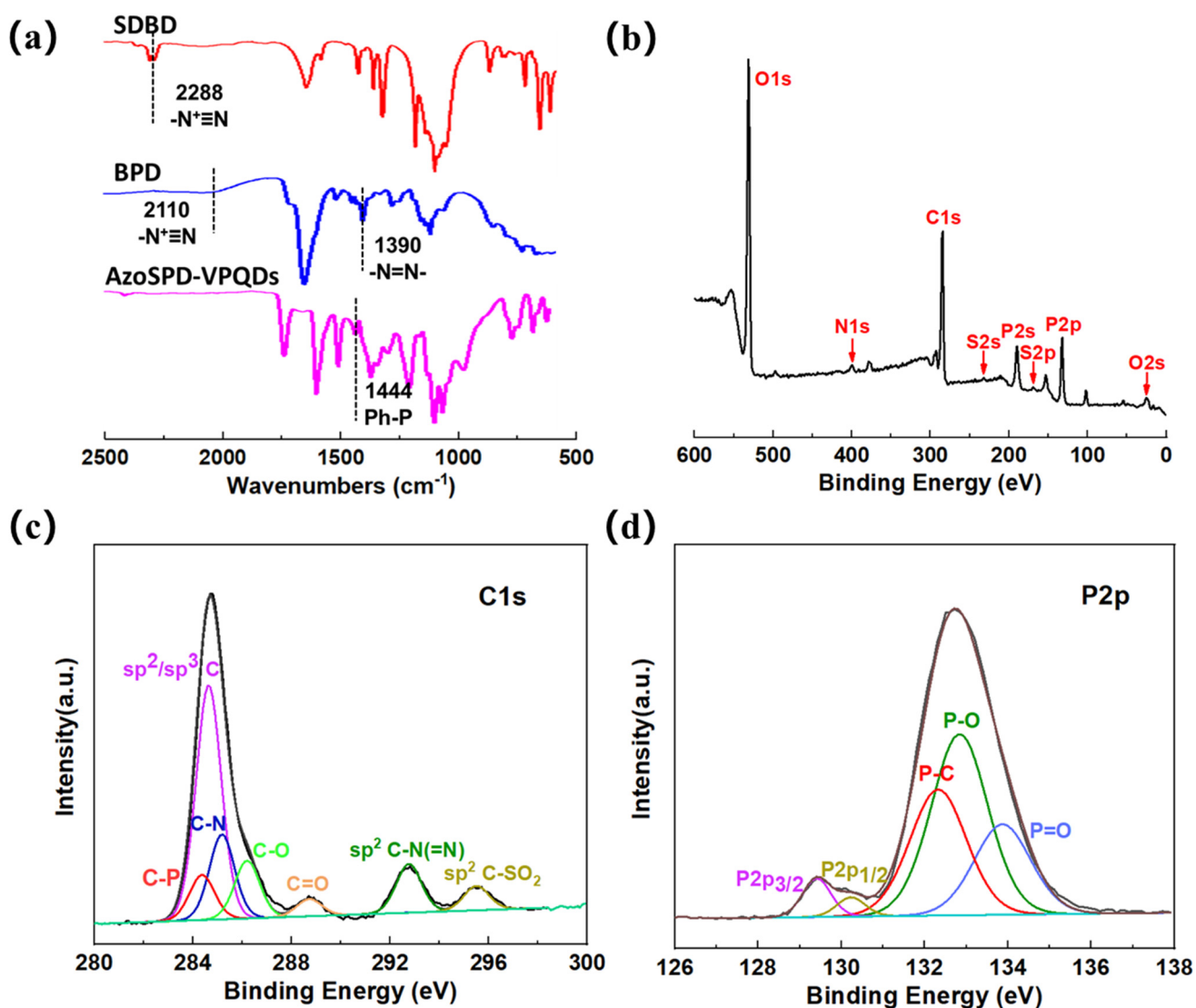


Figure 5. (a) IR spectrum characterization of SDBD, AzoSPD, and AzoSPD-VPQDs; (b) the XPS spectrum of AzoSPD-VPQDs in the binding energy range of 0–600 eV; (c) C1s high-resolution fine XPS spectrum of AzoSPD-VPQDs; (d) P2p high-resolution fine XPS spectrum of AzoSPD-VPQDs.

Fluorescence is one of the key detections based on the quantum confinement effect of quantum dot materials, and the intramolecular charge transfer processes occurring within the system may be closely related to the fluorescence quenching mechanism [9,25–27]. The liquid-phase ultraviolet–visible fluorescence emission spectrum of AzoSPD-VPQDs can be seen in Figure S3. The solid-state fluorescence excitation and emission spectra, which are more relevant to device behavior, are shown in Figure 6. The optimal excitation and

emission bands for the prepared VPQDs were measured at 358 and 440 nm, respectively. Their time-resolved fluorescence spectra (TRPL) fit a bi-exponential formula (see Figure 6 inset), expressed as:

$$y = y_0 + A_1 e^{-\frac{x}{\tau_1}} + A_2 e^{-\frac{x}{\tau_2}}$$

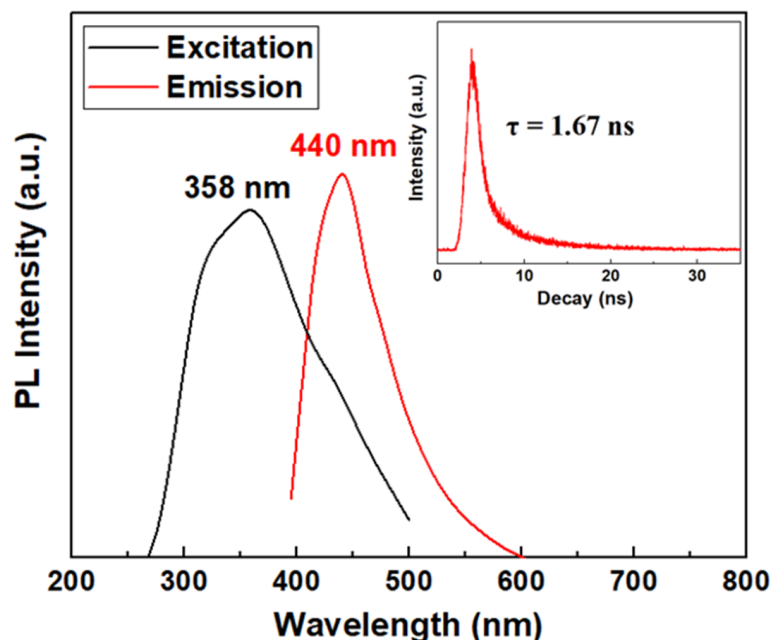


Figure 6. The fluorescence excitation (black line) and fluorescence emission (red line) spectra of AzoSPD-VPQDs.

The lifetimes of the AzoSPD-VPQD components are $\tau_1 = 1.28$ ns (93.02%) and $\tau_2 = 6.89$ ns (6.98%), from which the average lifetime (τ_{av}) is calculated to be 1.67 ns. The short-lifetime (τ_1) and the two longer-lifetime (τ_2) components arise from different emission sites on the VPQDs, corresponding to the fast- and slow-decay components, which are associated with the recombination at intrinsic states and defect states of the VPQDs, respectively [28].

The UV-Vis spectrum was used to reveal the photosensitive properties of the samples. Figure S4 displays the complete UV-Vis spectrum of AzoSPD within the 200–800 nm range, primarily comprising two strong absorption peaks. The peak at 250 nm is the $\pi-\pi^*$ transition peak on the phenyl group of azobenzene in the AzoSPD-conjugated system, and the maximum absorption peak at 440.75 nm is the $\pi-\pi^*$ electron transition absorption peak allowed by the symmetry between the two N atoms on the azobenzene [20]. The latter peak not only serves as the absorption band that initiates the configurational transition of azobenzene but also exhibits strong absorption characteristics indicative of considerable photoexcited electronic transition properties. Figure 7 compares the UV-Vis spectra of AzoSPD, VPQDs, and AzoSPD-VPQDs. AzoSPD-VPQDs exhibit a moderate maximum absorption peak at 441 nm, which is stronger than the peak of VPQDs at 433 nm, confirming that the modification has enhanced the light absorption of VPQDs. At the same time, the wavelength of AzoSPD-VPQDs is shorter than that of the pure AzoSPD molecule (458.4 nm) but longer than that of VPQDs (433 nm), reflecting the change in the chemical environment of VPQDs due to covalent modification. The introduction of the large conjugated system of the AzoSPD molecule makes the $\pi-\pi^*$ electronic transition in VPQDs more facile, which is distinct from conventional physical mixing methods (Figure S5 shows the comparison with UV-Vis physical mixing).

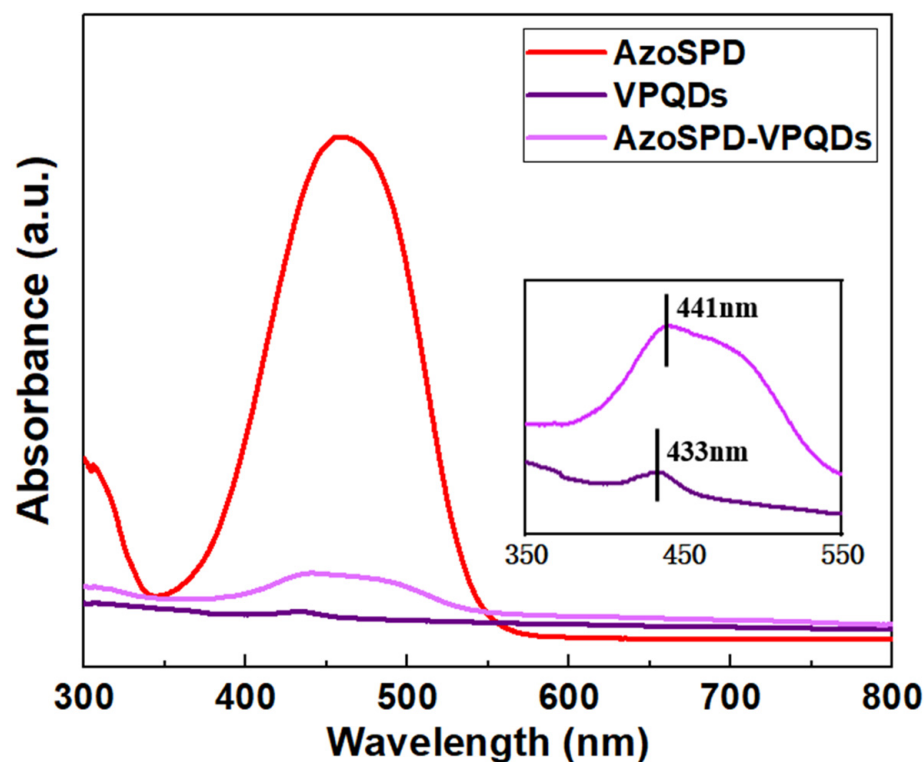


Figure 7. UV-Vis spectrum comparison of samples before and after modification. The inset is a local amplification image of VPQDs and AzoSPD-VPQDs at 350–550 nm.

In order to utilize the abundant photoresponsive azobenzene groups in AzoSPD, we investigated the photo-regulation conditions of AzoSPD-VPQDs by studying the temporal relationship between the duration of UV light exposure and the UV-Visible absorption spectra under 465 nm light conditions. For the solution state of AzoSPD-VPQDs, a persistent effect of the 465 nm light on the phenyl π - π^* transition absorption peak within the 200–250 nm range was observed, with the absorption intensity slightly increasing with prolonged exposure time, indicating a trend affected by the light (as shown in Figure S6). For the film state products, which have a more device-relevant light absorption effect (prepared by spin-coating), the relationship between the intensity of the main UV-Vis absorption peaks in the film and time is shown in Figure 8. The intensity of the π - π^* electronic transition absorption peak at 441 nm associated with the N=N bond in the film samples decreases with increasing light exposure time, while the intensity of the π electronic transition absorption peak of the benzene ring (at 298 nm) increases with exposure time. This suggests that under UV light, the waveform and intensity of the azobenzene gradually transition from the original E configuration to the Z configuration. Under prolonged continuous light exposure, there is little change in the spectrum, which may be related to the insufficient light intensity of the azobenzene in AzoSPD or large steric hindrance in the inversion space, but it also indirectly indicates the material's stability under UV light exposure.

3.2. Current–Voltage Characteristics and Performance Parameters

To test the application potential of modified VPQDs in the field of memristors, we constructed the Au/AzoSPD-VPQD/ITO structure device. Under the environmental conditions of 0~ \pm 3 V volt-ampere characteristic scanning, the cycle power scanning was carried out at a step frequency of 0.05 V and a limit current of 0.01 A. The device shows obvious memristive characteristics between the high-resistance state (HRS) and the low-resistance state (LRS) during the Set/Reset process of more than 90 cycles (Figure 9a). The power consumption during the switching process could be calculated from the I-V curve to be in the range of 10^{-8} to 10^{-5} W. The resistance of the HRS is

about $10^9 \Omega$, and the resistance of the LRS is about $10^6 \Omega$. The statistics of Set/Reset voltage show that the average Set voltage is 1.75 V, and the average Reset voltage is -1.52 V, with a standard deviation of 0.18 V and 0.37 V, respectively (Figure 9b). The average switch ratio of nearly 90 cycles at a voltage of 0.1 V is over 2×10^3 (Figure 9c). In contrast, the switch ratio of the device with AzoSPD or VPQDs as the functional layer is only 96.87 or 5.24 (the I–V scan curve of the control group can be seen in Figure S7). The time retention test is carried out under the condition that the reading voltage is 0.01 V and the time interval time is 0.4 s, and the high- and low-resistance states did not fluctuate greatly in the time of 1500 s (Figure 9d). It is worth mentioning that stability and repeatability are still the major disadvantages of current two-dimensional material-based memristors [29]; devices made by few-layer two-dimensional materials usually have difficulty achieving 100 switch cycles [30,31]. The presence of metal-free quantum dots coupled with the protective modification by AzoSPD confers good cycling performance on the device under environmental conditions [25,27,32]. Leveraging this advantage, a comparison of performance and power consumption between memristors based on metal and metal-free quantum dots is displayed in Table S1 (Supporting Information).

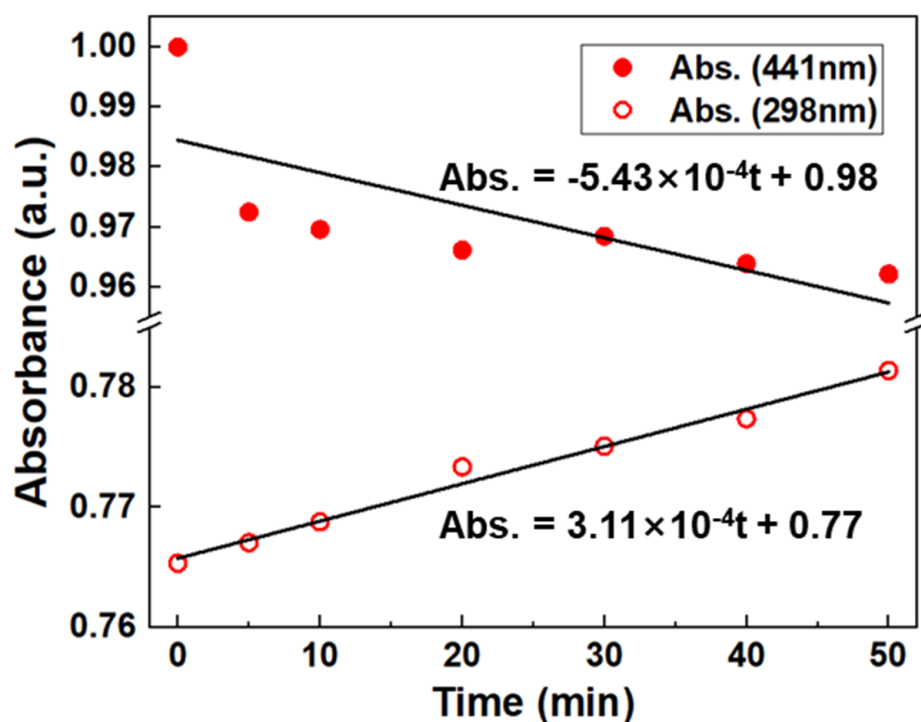


Figure 8. Time-dependent UV-Vis spectrum of AzoSPD-VPQDs under 465 nm light irradiation.

3.3. Photo Response Characteristics

The abundant photosensitive group azobenzene in AzoSPD provides an additional optical control method for the device. Compared with the HRS current in the dark, the HRS readout current of the Au/AzoSPD-VPQD/ITO device increases by nearly 40 times after 20 min of 465 nm light irradiation, while the LRS readout current also increases by 1.4 times (Figure 10). It means that the 465 nm light can significantly reduce the switching ratio of the device, reflecting the device's ability to sense light signals and store information. Given the quenching behavior of QDs in solid-state films, the photo-storage behavior of the device is mainly associated with the bandgap changes induced by the photo-induced configurational transition of azobenzene in AzoSPD and the photo-excited electrons.

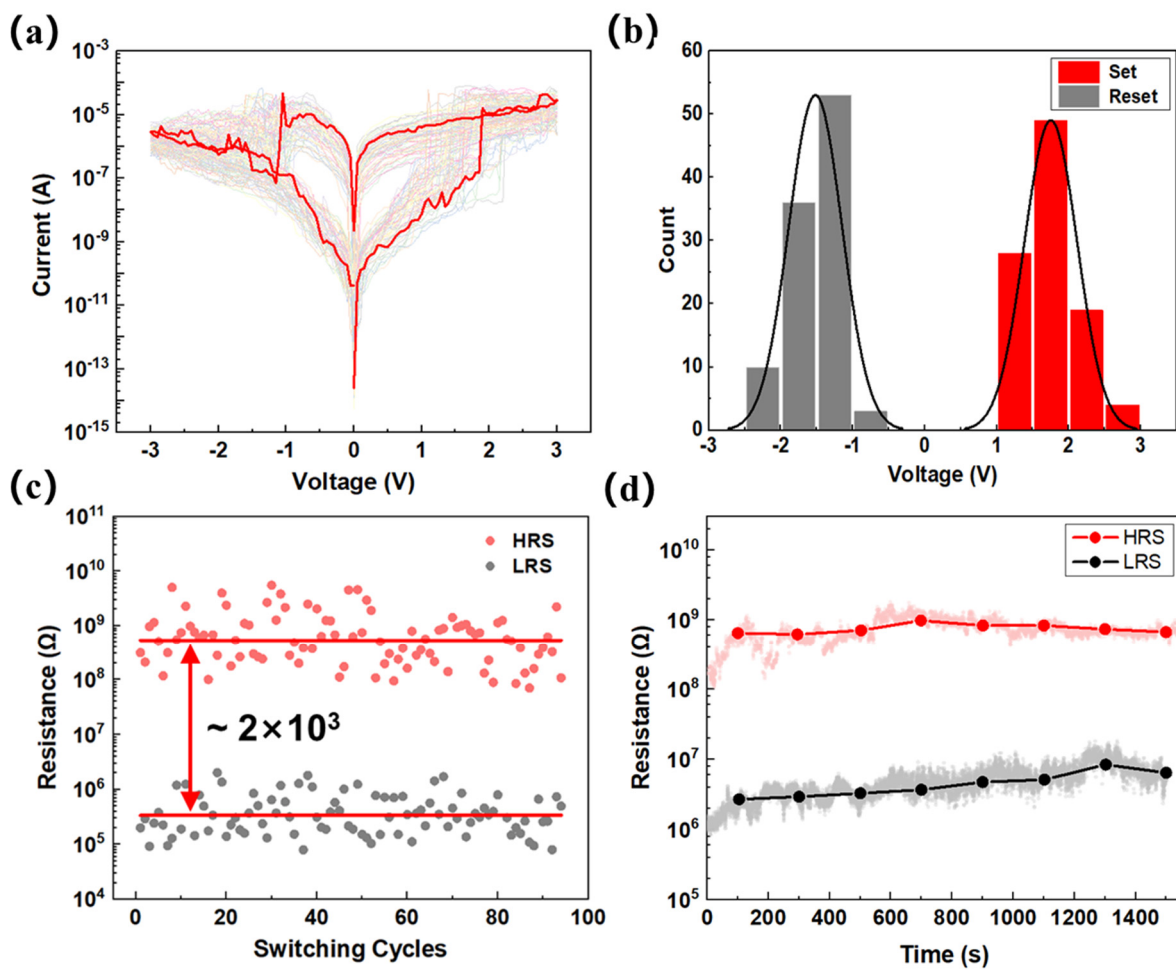


Figure 9. (a) The memristive characteristic curve of the Au/AzoSPD-VPQD/ITO device; (b) Set/Reset voltage statistics of the device; (c) cycle stability test of the device; (d) time retention test of the device.

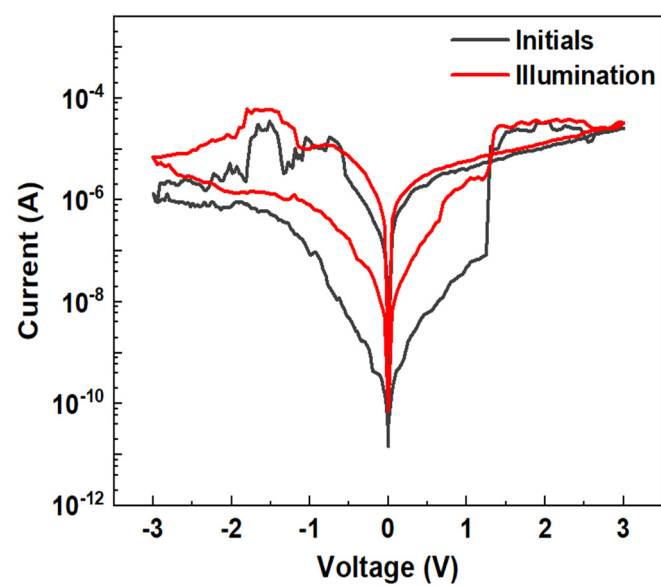


Figure 10. The average change of the I-V characteristic curve after 465 nm irradiation for 20 min.

3.4. Mechanism Explanation

To further detail the conversion mechanism of the device, the density functional theory (DFT) calculation of the AzoSPD–VPQD structural unit is performed in Gaussian09 using the B3LYP mixing function method and the 6–31G(d) basis set. The result of the optimization is shown in Figure 11a, and the structural unit of AzoSPD–VPQDs selects the AzoSPD monomer (the other two sites of TBTC are filled with SDBD) and the VP unit which directly connects to AzoSPD. Additionally, the unmodified SDBD terminal diazo group is removed to maintain the system’s electrical neutrality. The Molecular Electrostatic Potential (ESP) diagram, shown in Figure 11b, depicts the distribution of electrostatic potential within the molecule, and the VP part shows a higher electronegativity that can be used to capture the delocalized π electron during AzoSPD excitation. The HOMO and LUMO orbital shapes of AzoSPD–VPQDs are plotted by using the single point energy calculation results (Figure 11c,d). In the HOMO, the wave function is mainly concentrated on the AzoSPD side, while in the LUMO, the wave function is distributed in the VP region. When AzoSPD–VPQDs get excited, AzoSPD acts as an electron donor, and the HOMO electron is delocalized and transfers to VP along the chemical bond to generate the charge transfer state (AzoSPD⁺–VPQDs[−]). This allows VP to have additional electrons to trigger electronic conductance and obtain better conductivity. During the memristive test, the change in HRS current at low voltage adheres to Ohm’s law. But when the voltage gradually increases to the electrical excitation threshold of AzoSPD–VPQDs (1.75 V), the appearance of the charge transfer state (AzoSPD⁺–VPQDs[−]) transforms the device from HRS to LRS until the reverse voltage is large enough (−1.52 V) to re-extract the electrons back to the VP part and return to HRS.

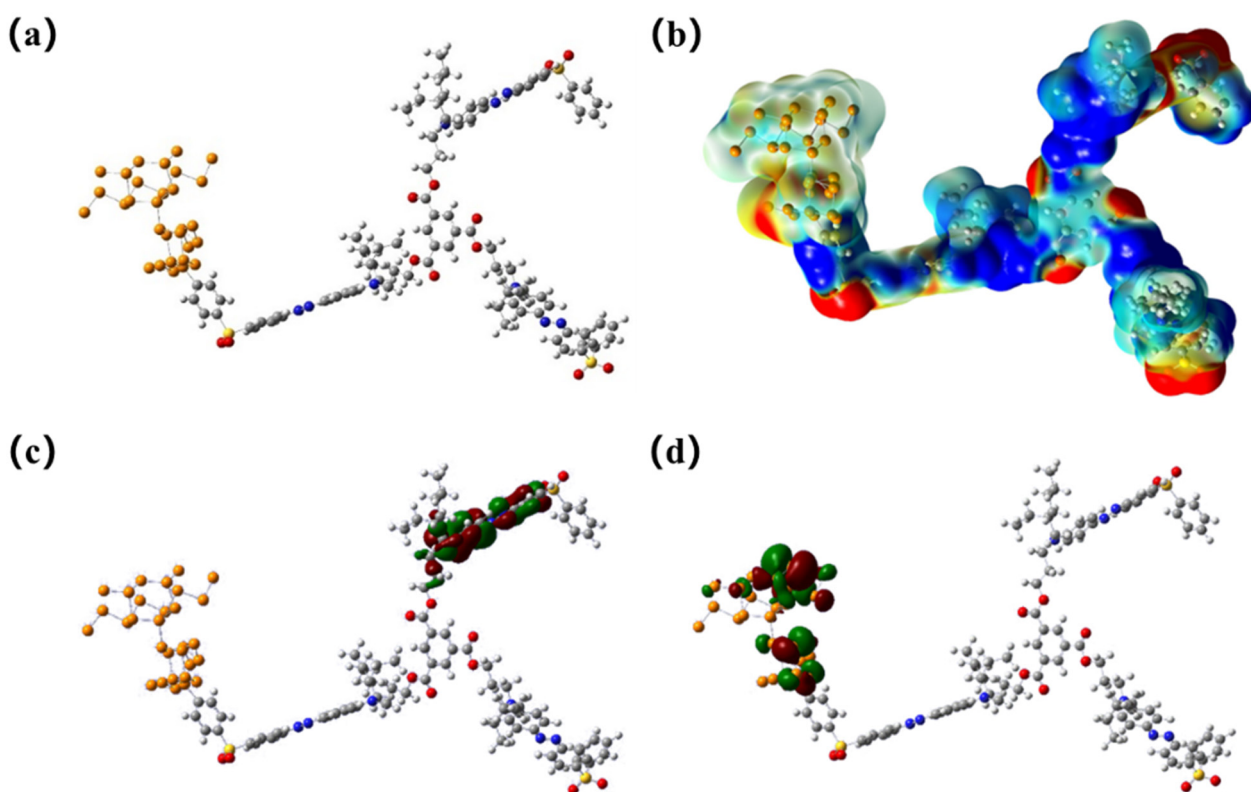


Figure 11. The Gaussian theoretical calculation of AzoSPD–VPQD monomer. (a) Structural optimization result of AzoSPD–VPQDs; (b) ESP distribution map of AzoSPD–VPQDs; (c) the HOMO orbital shape of AzoSPD–VPQDs; (d) the LUMO orbital shape of AzoSPD–VPQDs.

Under the exposure of 465 nm light, the change in current value can be mainly attributed to the photosensitive characteristic of AzoSPD. Due to the strong absorption in the

UV-Vis spectrum, 465 nm light can provide enough transition energy for the ground-state electron of AzoSPD-VPQDs so that the electron in some molecules is excited in advance to form the charge transfer state ($\text{AzoSPD}^+-\text{VPQDs}^-$) and results in a higher HRS current. At the same time, the small-scale configuration transition induced by UV light may also make the charge delocalization easier, reducing the bandgap energy difference, thereby enhancing the degree of charge transfer, which results in a slight increase in the LRS current. The aforementioned results demonstrate the controllable photoelectric improvement characteristics of AzoSPD chemical modification on VP, providing a preliminary exploration for the multi-modal regulation of memristive ability.

4. Conclusions

In summary, we have successfully synthesized a star-shaped polymer diazonium salt rich in azobenzene structure (AzoSPD) and grafted it to VPQDs through C-P covalent bonds. This is the first study to explore a modified composite material based on VPQDs as a photosensitive functional layer in memristors. The prepared Au/AzoSPD-VPQD/ITO memristor exhibited remarkable memory characteristics under ambient conditions, with a stable cycle number of over 90 times, a switching ratio exceeding 2×10^3 , and a retention time of 1500 s. Under 465 nm illumination, the HRS current can also be increased by nearly 40 times, enabling optical signal perception and storage. The mechanism of charge transfer explains the tunable optoelectronic properties through the Gaussian theory calculation fitting results in combination with the material properties of azobenzene. This research investigates the modification method of VPQDs and its application potential in memristors, providing insights into the development of photoelectric tunable devices based on the charge transfer mechanism.

Supplementary Materials: The following supporting information can be downloaded at: <https://www.mdpi.com/article/10.3390/pr1123429/s1>, Figure S1. (a) The SEM characterization of the device is ITO, AzoSPD-VPQDs, and Au, with thicknesses of 180, 120, and 80 nm, respectively. (b) EDS analysis under SEM characterization. Figure S2. The height distribution map of the AFM along the two lines. Figure S3. The fluorescence emission spectrum of the AzoSPD-VPQDs solution at 360 nm excitation. Figure S4. UV-Vis spectrum of AzoSPD in the range of 200–800 nm. Figure S5. UV-Vis contrast diagram of chemical modification and physical mixing. Where '@' represents physical mixing and '-' represents chemical bonding. Figure S6. The UV-Vis absorption peak intensity of the AzoSPD-VPQDs solution changed with the irradiation time under 465 nm light irradiation (200–250 nm). Figure S7. The memristive characteristic curve of the control group, (a) Au/AzoSPD/ITO structure device; (b) Au/VPQDs/ITO structure device. Table S1. The performance of this work compared with some QDs memristors. Refs. [9,25,27,33–35] are cited in the Supplementary Materials.

Author Contributions: Conceptualization, F.S. and W.C.; methodology, F.S. and W.C.; validation, F.S.; formal analysis, F.S.; investigation, F.S. and W.C.; resources, W.C. and G.L.; data curation, F.S.; writing—original draft preparation, F.S.; writing—review and editing, W.C. and G.L.; visualization, F.S.; supervision, W.C. and G.L.; project administration, G.L.; funding acquisition, G.L. All authors have read and agreed to the published version of the manuscript.

Funding: This research was funded by the National Key R&D Program of China (2022YFB4700102) and the National Natural Science Foundation of China (62111540271, 61974090).

Data Availability Statement: Data are contained within the article.

Conflicts of Interest: The authors declare no conflict of interest.

References

1. Zhou, K.; Shang, G.; Hsu, H.; Han, S.; Roy, V.A.L.; Zhou, Y. Emerging 2D Metal Oxides: From Synthesis to Device Integration. *Adv. Mater.* **2023**, *35*, 2207774. [[CrossRef](#)] [[PubMed](#)]
2. Sangwan, V.K.; Lee, H.-S.; Bergeron, H.; Balla, I.; Beck, M.E.; Chen, K.-S.; Hersam, M.C. Multi-Terminal Memtransistors from Polycrystalline Monolayer Molybdenum Disulfide. *Nature* **2018**, *554*, 500–504. [[CrossRef](#)] [[PubMed](#)]
3. García De Arquer, F.P.; Talapin, D.V.; Klimov, V.I.; Arakawa, Y.; Bayer, M.; Sargent, E.H. Semiconductor Quantum Dots: Technological Progress and Future Challenges. *Science* **2021**, *373*, eaaz8541. [[CrossRef](#)] [[PubMed](#)]

4. Yan, X.; Pei, Y.; Chen, H.; Zhao, J.; Zhou, Z.; Wang, H.; Zhang, L.; Wang, J.; Li, X.; Qin, C.; et al. Self-Assembled Networked PbS Distribution Quantum Dots for Resistive Switching and Artificial Synapse Performance Boost of Memristors. *Adv. Mater.* **2019**, *31*, 1805284. [[CrossRef](#)] [[PubMed](#)]
5. Wang, C.; He, W.; Tong, Y.; Zhang, Y.; Huang, K.; Song, L.; Zhong, S.; Ganeshkumar, R.; Zhao, R. Memristive Devices with Highly Repeatable Analog States Boosted by Graphene Quantum Dots. *Small* **2017**, *13*, 1603435. [[CrossRef](#)] [[PubMed](#)]
6. Zhang, X.; Xie, H.; Liu, Z.; Tan, C.; Luo, Z.; Li, H.; Lin, J.; Sun, L.; Chen, W.; Xu, Z.; et al. Black Phosphorus Quantum Dots. *Angew. Chem. Int. Ed.* **2015**, *54*, 3653–3657. [[CrossRef](#)]
7. Wang, Y.; Wu, F.; Liu, X.; Lin, J.; Chen, J.-Y.; Wu, W.-W.; Wei, J.; Liu, Y.; Liu, Q.; Liao, L. High on/off Ratio Black Phosphorus Based Memristor with Ultra-Thin Phosphorus Oxide Layer. *Appl. Phys. Lett.* **2019**, *115*, 193503. [[CrossRef](#)]
8. Han, S.-T.; Hu, L.; Wang, X.; Zhou, Y.; Zeng, Y.-J.; Ruan, S.; Pan, C.; Peng, Z. Black Phosphorus Quantum Dots with Tunable Memory Properties and Multilevel Resistive Switching Characteristics. *Adv. Sci.* **2017**, *4*, 1600435. [[CrossRef](#)]
9. Cao, Y.; Zhang, B.; Tian, X.; Gu, M.; Chen, Y. Direct Covalent Modification of Black Phosphorus Quantum Dots with Conjugated Polymers for Information Storage. *Nanoscale* **2019**, *11*, 3527–3533. [[CrossRef](#)]
10. He, C.L.; Zhuge, F.; Zhou, X.F.; Li, M.; Zhou, G.C.; Liu, Y.W.; Wang, J.Z.; Chen, B.; Su, W.J.; Liu, Z.P.; et al. Nonvolatile Resistive Switching in Graphene Oxide Thin Films. *Appl. Phys. Lett.* **2009**, *95*, 232101. [[CrossRef](#)]
11. Rehman, M.M.; Siddiqui, G.U.; Gul, J.Z.; Kim, S.-W.; Lim, J.H.; Choi, K.H. Resistive Switching in All-Printed, Flexible and Hybrid MoS₂-PVA Nanocomposite Based Memristive Device Fabricated by Reverse Offset. *Sci. Rep.* **2016**, *6*, 36195. [[CrossRef](#)]
12. Qian, K.; Tay, R.Y.; Nguyen, V.C.; Wang, J.; Cai, G.; Chen, T.; Teo, E.H.T.; Lee, P.S. Hexagonal Boron Nitride Thin Film for Flexible Resistive Memory Applications. *Adv. Funct. Mater.* **2016**, *26*, 2176–2184. [[CrossRef](#)]
13. Xie, Z.; Zhang, B.; Ge, Y.; Zhu, Y.; Nie, G.; Song, Y.; Lim, C.-K.; Zhang, H.; Prasad, P.N. Chemistry, Functionalization, and Applications of Recent Monoelemental Two-Dimensional Materials and Their Heterostructures. *Chem. Rev.* **2022**, *122*, 1127–1207. [[CrossRef](#)]
14. Zhang, L.; Huang, H.; Zhang, B.; Gu, M.; Zhao, D.; Zhao, X.; Li, L.; Zhou, J.; Wu, K.; Cheng, Y.; et al. Structure and Properties of Violet Phosphorus and Its Phosphorene Exfoliation. *Angew. Chem. Intl. Edit.* **2020**, *59*, 1074–1080. [[CrossRef](#)]
15. Chen, J.; Wang, C.; Li, H.; Xu, X.; Yang, J.; Huo, Z.; Wang, L.; Zhang, W.; Xiao, X.; Ma, Y. Recent Advances in Surface Modifications of Elemental Two-Dimensional Materials: Structures, Properties, and Applications. *Molecules* **2022**, *28*, 200. [[CrossRef](#)]
16. Liao, K.; Lei, P.; Tu, M.; Luo, S.; Jiang, T.; Jie, W.; Hao, J. Memristor Based on Inorganic and Organic Two-Dimensional Materials: Mechanisms, Performance, and Synaptic Applications. *ACS Appl. Mater. Interfaces* **2021**, *13*, 32606–32623. [[CrossRef](#)]
17. Cao, Y.; Tian, X.; Gu, J.; Liu, B.; Zhang, B.; Song, S.; Fan, F.; Chen, Y. Covalent Functionalization of Black Phosphorus with Conjugated Polymer for Information Storage. *Angew. Chem. Int. Ed.* **2018**, *57*, 4543–4548. [[CrossRef](#)]
18. Liu, Y.; Gao, P.; Zhang, T.; Zhu, X.; Zhang, M.; Chen, M.; Du, P.; Wang, G.; Ji, H.; Yang, J.; et al. Azide Passivation of Black Phosphorus Nanosheets: Covalent Functionalization Affords Ambient Stability Enhancement. *Angew. Chem. Int. Ed.* **2019**, *58*, 1479–1483. [[CrossRef](#)]
19. Ryder, C.R.; Wood, J.D.; Wells, S.A.; Yang, Y.; Jariwala, D.; Marks, T.J.; Schatz, G.C.; Hersam, M.C. Covalent Functionalization and Passivation of Exfoliated Black Phosphorus via Aryl Diazonium Chemistry. *Nat. Chem.* **2016**, *8*, 597–602. [[CrossRef](#)]
20. Hamon, F.; Djedaini-Pilard, F.; Barbot, F.; Len, C. Azobenzenes—Synthesis and Carbohydrate Applications. *Tetrahedron* **2009**, *65*, 10105–10123. [[CrossRef](#)]
21. Sun, J.; Chen, Q.; Fan, F.; Zhang, Z.; Han, T.; He, Z.; Wu, Z.; Yu, Z.; Gao, P.; Chen, D.; et al. A Dual-Mode Organic Memristor for Coordinated Visual Perceptive Computing. *Fundam. Res.* **2022**, S266732582200303X. [[CrossRef](#)]
22. Zhou, Y.; Qi, H.; Yang, J.; Bo, Z.; Huang, F.; Islam, M.S.; Lu, X.; Dai, L.; Amal, R.; Wang, C.H.; et al. Two-Birds-One-Stone: Multifunctional Supercapacitors beyond Traditional Energy Storage. *Energy Environ. Sci.* **2021**, *14*, 1854–1896. [[CrossRef](#)]
23. Huang, Y.; Zhu, M.; Huang, Y.; Pei, Z.; Li, H.; Wang, Z.; Xue, Q.; Zhi, C. Multifunctional Energy Storage and Conversion Devices. *Adv. Mater.* **2016**, *28*, 8344–8364. [[CrossRef](#)]
24. Zhao, R.; Zhao, X.; Xu, X.; Zhang, Y.; Wang, Y.; Jin, M.; Liu, Z.; Cheng, Y.; Zheng, H.; Zhang, J. Wide Bandgap Tuning of Violet Phosphorus Quantum Dots by Functionalization. *J. Phys. Chem. Lett.* **2022**, *13*, 8236–8244. [[CrossRef](#)]
25. Ali, M.; Sokolov, A.; Ko, M.J.; Choi, C. Optically Excited Threshold Switching Synapse Characteristics on Nitrogen-Doped Graphene Oxide Quantum Dots (N-GOQDs). *J. Alloy Compd.* **2021**, *855*, 157514. [[CrossRef](#)]
26. Sokolov, A.; Ali, M.; Li, H.; Jeon, Y.; Ko, M.J.; Choi, C. Partially Oxidized MXene Ti₃C₂T_x Sheets for Memristor Having Synapse and Threshold Resistive Switching Characteristics. *Adv. Elect. Mater.* **2021**, *7*, 2000866. [[CrossRef](#)]
27. Sokolov, A.S.; Ali, M.; Riaz, R.; Abbas, Y.; Ko, M.J.; Choi, C. Silver-Adapted Diffusive Memristor Based on Organic Nitrogen-Doped Graphene Oxide Quantum Dots (N-GOQDs) for Artificial Biosynapse Applications. *Adv. Funct. Mater.* **2019**, *29*, 1807504. [[CrossRef](#)]
28. Zhao, R.; Liu, S.; Zhao, X.; Cheng, Y.; Zhang, J. Violet Phosphorus Quantum Dots as Distinguishable Environmental Biosensors. *Adv. Mater. Inter.* **2022**, *9*, 2200705. [[CrossRef](#)]
29. Huh, W.; Lee, D.; Lee, C. Memristors Based on 2D Materials as an Artificial Synapse for Neuromorphic Electronics. *Adv. Mater.* **2020**, *32*, 2002092. [[CrossRef](#)]
30. Ge, R.; Wu, X.; Kim, M.; Shi, J.; Sonde, S.; Tao, L.; Zhang, Y.; Lee, J.C.; Akinwande, D. Atomristor: Nonvolatile Resistance Switching in Atomic Sheets of Transition Metal Dichalcogenides. *Nano Lett.* **2018**, *18*, 434–441. [[CrossRef](#)]

31. Zhang, W.; Gao, H.; Deng, C.; Lv, T.; Hu, S.; Wu, H.; Xue, S.; Tao, Y.; Deng, L.; Xiong, W. An Ultrathin Memristor Based on a Two-Dimensional WS₂/MoS₂ Heterojunction. *Nanoscale* **2021**, *13*, 11497–11504. [[CrossRef](#)] [[PubMed](#)]
32. Chen, W.; Gao, S.; Xie, Z.; Lu, Y.; Gong, G.; Liu, G.; Shang, J.; Yao, C.; Li, R.-W. Anti-Oxidative Passivation and Electrochemical Activation of Black Phosphorus *via* Covalent Functionalization and Its Nonvolatile Memory Application. *J. Mater. Chem. C* **2020**, *8*, 7309–7313. [[CrossRef](#)]
33. Ren, S.; Li, Z.; Liu, X.; Li, Y.; Cao, G.; Zhao, J. Oxygen Migration Induced Effective Magnetic and Resistive Switching Boosted by Graphene Quantum Dots. *J. Alloys Compd.* **2021**, *863*, 158339. [[CrossRef](#)]
34. Bokka, N.; Adepu, V.; Selamneni, V.; Sahatiya, P. Non-Contact, Controlled and Moisture Triggered Black Phosphorus Quantum Dots/PVA Film for Transient Electronics Applications. *Mater. Lett.* **2021**, *290*, 129477. [[CrossRef](#)]
35. Wang, J.; Lv, Z.; Xing, X.; Li, X.; Wang, Y.; Chen, M.; Pang, G.; Qian, F.; Zhou, Y.; Han, S.-T. Optically Modulated Threshold Switching in Core-Shell Quantum Dot Based Memristive Device. *Adv. Funct. Mater.* **2020**, *30*, 1909114. [[CrossRef](#)]

Disclaimer/Publisher's Note: The statements, opinions and data contained in all publications are solely those of the individual author(s) and contributor(s) and not of MDPI and/or the editor(s). MDPI and/or the editor(s) disclaim responsibility for any injury to people or property resulting from any ideas, methods, instructions or products referred to in the content.